




Effect of Texture Region on the Static and Dynamic Characteristic of Partially Textured Journal Bearings

Hiroo Taura 

Nagaoka University of Technology, 1603-1, Kamitomioka,
Nagaoka, Niigata 940-2188, Japan
htauration@mech.nagaokaut.ac.jp

Abstract. The effect of the texturing region on the static and dynamic characteristics of partially textured bearings, of which the texturing area is limited on the bearing surface in the circumferential direction, were investigated theoretically. The load carrying capacity and stiffness and damping coefficients of some partially textured journal bearings with the different textured region were calculated by using a numerical model considering the effects of both fluid inertia and energy loss at the edges of the dimples. The results showed that when the surface texturing was formed in the unloaded region of the journal bearing surface, the load carrying capacity maintains as much as the smooth bearing for a wide range of Sommerfeld number. The linear stability threshold speeds of a symmetrical rigid rotor supported in two identical textured bearings was also calculated with the dynamic coefficients of the oil film. The results obtained showed that when the texture region starts from 270° from the top of the bearing in the rotating direction, the stability threshold speeds are higher than those of the fully textured bearing at relatively high Sommerfeld number. From these results, it was concluded that an appropriate partial texturing formed on the bearing surface can improve both the load carrying capacity and the stability characteristics simultaneously.

Keywords: Journal bearing · Surface texture · Load carrying capacity
Stability

Nomenclature

C	Mean radial clearance
D	Bearing diameter ($=2R$)
L	Bearing length
N	Journal rotational speed
O_b, O_j	Origin of bearing or journal
R	Bearing inner radius
S	Sommerfeld number
W	Static load
X, Y	Vertical and horizontal axes
e	Eccentricity
f_x, f_y	Oil-film-force components in the vertical and horizontal directions

H	Dimensionless oil-film-thickness
h_t	Depth of square dimple
$l_{tz}, l_{t\theta}$	Width of square dimples in the axial and circumferential directions
$l_{pz}, l_{p\theta}$	Pitch of square dimples in the axial and circumferential directions
m	Half of mass of a model rotor
P	Oil film pressure (above ambient)
x, z	Coordinates in the circumferential and axial directions
δ	Ratio of dimple depth to mean radial clearance ($=h_t/C_r$)
ε	Eccentricity ratio ($=e/C$)
η	Viscosity of fluid
θ	Angular coordinate ($=x/R$)
θ_t	Start angle of texture region
θ_{ts}	Circumferential angle of texture region
ϕ	Attitude angle, deg
ω	Journal angular velocity, rad/s

1 Introduction

Surface texturing has been applied to various mechanical elements with the mating surfaces for the improvement of lubrication performance. This technique has also attracted attention in a field of the journal bearings, and many researchers have investigated the effect of surface texturing on the static characteristics of journal bearings [1–10]. The present authors [11, 12] have also analyzed numerically and experimentally the load carrying capacity and dynamic coefficients of textured journal bearings with square dimples. They proposed a numerical model considering both effects of the fluid inertia and the energy loss at the edge of dimples, and the results agreed qualitatively and quantitatively with the experimental ones, confirming the validity of the numerical model. They also demonstrated that the fully textured bearings improve the stability of a rotor supported in the bearings, but decrease the load carrying capacity. As for the load carrying capacity, Tala-Ighil et al. [1] and Brizmer [5] also revealed that the load carrying capacity was increased by manufacturing an appropriate texturing area on the bearing surface, but they have not investigated the dynamic characteristic of the bearings.

In the study, we focus on the partially textured bearings, of which the texturing area is limited on the bearing surface in the circumferential direction, and numerically investigate the effect of the texturing region on the static and dynamic characteristics of the bearings.

2 Numerical Analysis

2.1 Analytical Model

Figure 1 shows a partially textured journal bearing used in this analysis. The journal rotates with a rotational speed ω about its axis, which locates at the static equilibrium position with eccentricity e and attitude angle ϕ . The static load W is applied to the journal vertically downward. A Cartesian coordinate system is also shown in Fig. 1. The x -axis is along the vertical direction, the z -axis is in the direction of the journal length, and the Y axis is perpendicular to the x - and z -axes. The circumferential coordinate θ is measured from the positive X axis in the rotating direction. An axial oil groove is set on the top of the bearing and lubricating oil is supplied from it. The texture region is formed from θ_{ts} to $\theta_{ts} + \theta_s$ on the bearing surface in the circumferential direction, and to the whole in the axial direction.

Figure 2 shows a schematic of the dimples on the bearing surface. We chose the square dimples according to our previous study [11, 12]. As shown in Fig. 1, the square dimples are formed at an equal interval in the texture region. Three parameters characterize the square dimples; the depth h_d , the length and the pitch. Considering the direction, the length are represented $l_{d\theta}$, l_{dz} in the circumferential and axial direction respectively, and the pitch $l_{p\theta}$, l_{pz} in the circumferential and axial direction respectively.

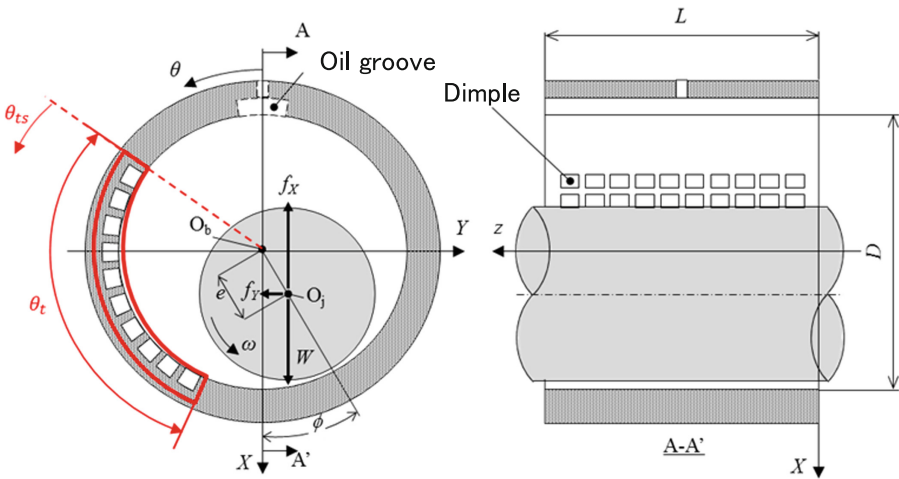


Fig. 1. Analytical model of the partially textured journal bearing with a coordinate system

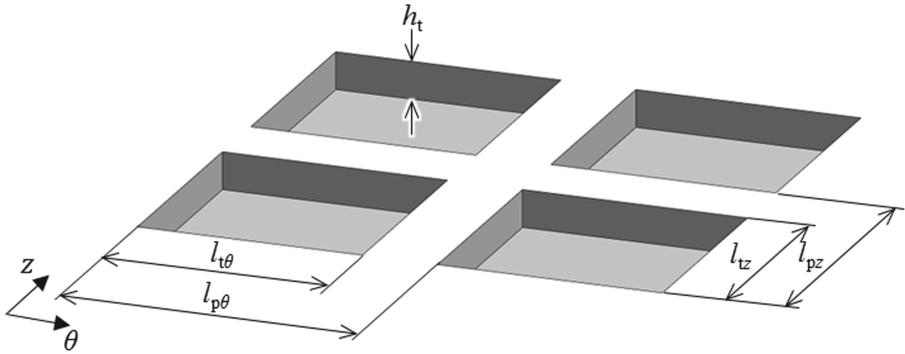


Fig. 2. Schematic view of the square dimples [11]

2.2 Governing Equation for the Pressure Distribution

As the calculation procedure used in the study were almost similar to the reference [11, 12], we described it briefly here.

In the study, the pressure distribution of the oil film is determined based on the Reynolds equation, considering the inertia effect and the energy loss due to the film discontinuity at the edge of dimples. In this study, the pressure jump due to the inertial effect is evaluated by using Bernoulli’s equation and the energy loss is calculated using expressions that depend upon film expansion or contraction.

As the governing equation for the pressure distribution, we used the incompressible and iso-viscous Reynolds equation written in dimensionless form as follows:

$$\frac{\partial}{\partial \theta} \left(H^3 \frac{\partial P}{\partial \theta} \right) + \frac{1}{4} \left(\frac{D}{L} \right)^2 \frac{\partial}{\partial Z} \left(H^3 \frac{\partial P}{\partial Z} \right) = 6 \frac{\partial H}{\partial \theta} + 12 \frac{\partial H}{\partial \tau} \tag{1}$$

The dimensionless forms of the variables in Eq. (1) are defined in Eq. (2):

$$\theta = \frac{x}{R}, Z = \frac{z}{L}, H = \frac{h}{C}, P = \frac{p}{\eta \omega} \left(\frac{C}{R} \right)^2, \tau = \omega t \tag{2}$$

The dimensionless film thickness in the land is given by

$$H = 1 + \varepsilon \cos(\theta - \phi) \tag{3}$$

and in the dimple

$$H = 1 + \varepsilon \cos(\theta - \phi) + \delta \tag{4}$$

where $\varepsilon (=e/C)$ is the eccentricity ratio and $\delta (=h_t/C)$ is the dimple-depth ratio.

The inertia effect and energy loss of the fluid in the discontinuous clearance at the edge of the dimples are evaluated by using a combination of Bernoulli’s equation and

some loss formula. At a film-expansion point, the loss formula of a sudden expansion pipe is applied to estimate the pressure variation:

$$p^- - p^+ = \frac{\rho}{2} \left((u^{*+})^2 - (u^{*-})^2 \right) + \xi_{\text{loss}} \cdot \frac{\rho}{2} (u^{*-})^2 \tag{5}$$

Where, u^* denotes the average fluid velocity in the film-thickness direction, and the superscripts + and - indicate quantities in the dimple section just after flowing out of the smooth section and quantities in the smooth section just before entering a dimple, respectively. The coefficient of loss, ξ , is defined as

$$\xi_{\text{loss}} = \zeta \left(1 - \frac{h^-}{h^+} \right)^2 \tag{6}$$

where ζ is 1.0 in the study [11]. At an abrupt reduction point, the empirical formula [13] of step bearings is used.

$$p^- - p^+ = \beta \frac{\rho}{2} \left((u^{*+})^2 - (u^{*-})^2 \right) + \zeta_1 \frac{\rho}{2} \left((u^{*+})^2 - (u^{*-})^2 \right) - \zeta_2 \rho U^2 \ln \frac{h^-}{h^+} \tag{7}$$

In the laminar regime, coefficient β takes a value of 1.2 and coefficients ζ_1 and ζ_2 each take values of 0.133 [13].

As the boundary conditions for pressure, Reynolds boundary condition is applied. The pressures at both bearing ends and in the oil-feeding groove were set to zero (ambient pressure).

After the pressure distribution was obtained, the vertical and horizontal components of the oil-film reaction force can, respectively, be calculated by the following integrals:

$$f_X = -\eta\omega \left(\frac{R}{C} \right)^2 RL \int_0^1 \int_0^{2\pi} P \cos \theta d\theta dZ \tag{8}$$

$$f_Y = -\eta\omega \left(\frac{R}{C} \right)^2 RL \int_0^1 \int_0^{2\pi} P \sin \theta d\theta dZ \tag{9}$$

The above two force components under the steady state condition, f_{X0} and f_{Y0} , are as follows:

$$f_{X0} = W \tag{10}$$

$$f_{Y0} = 0 \tag{11}$$

where W is the static load applied vertically downward on the journal.

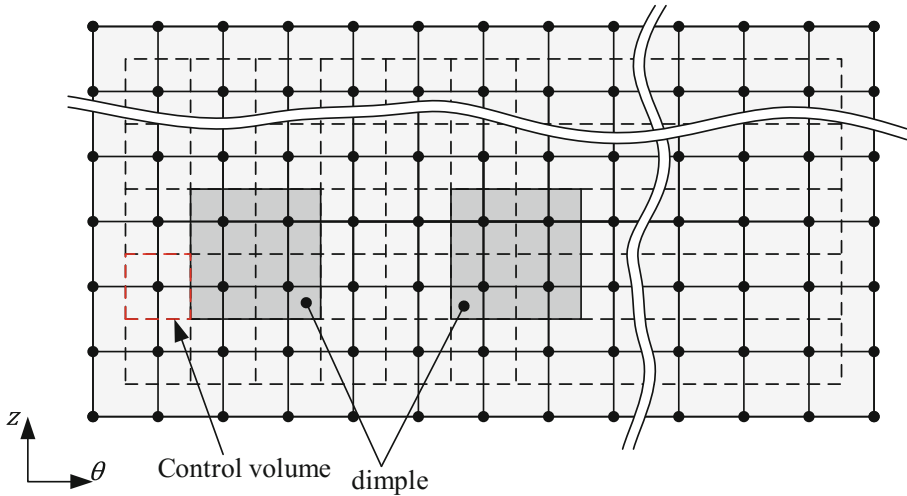


Fig. 3. Discretization of the bearing surface

2.3 Numerical Calculation of the Pressure Distribution

To obtain the pressure distribution numerically, the Reynolds Eq. (1) was discretized by using a cell method, which is proposed by Arghir [14]. The calculation region is divided into an orthogonal grid with 180 in the circumferential direction by 60 across the bearing width, and the edges of the square dimple are placed on the cell boundary as shown in Fig. 3. The pressures at the cell's centers are calculated with a difference equation derived from Eq. (1) using a successive over-relaxation scheme, whereas the pressures at the cell boundaries on the step between the dimple and the smooth region are also calculated considering the inertia effect and the energy loss. If any negative pressures obtained during the iteration, the pressure are set to zero to maintain the Reynolds boundary conditions.

2.4 Calculation of the Dynamic Coefficients of the Oil Film

When the rotor is applied small displacements, ΔX and ΔY , and small velocities, $\Delta \dot{X}$ and $\Delta \dot{Y}$, in vertical and horizontal directions around its equilibrium position, the dynamic reacting forces, f_X and f_Y , are described with eight dynamic coefficients based on the assumption of linearization as follows:

$$\begin{cases} f_X = f_{X0} + k_{XX}\Delta X + k_{XY}\Delta Y + c_{XX}\Delta \dot{X} + c_{XY}\Delta \dot{Y} \\ f_Y = f_{Y0} + k_{YX}\Delta X + k_{YY}\Delta Y + c_{YX}\Delta \dot{X} + c_{YY}\Delta \dot{Y} \end{cases} \quad (12)$$

where k_{ij} and c_{ij} ($i, j = X, Y$) are the stiffness and damping coefficients, respectively. Stiffness and damping coefficients are defined as follows:

$$\begin{bmatrix} k_{XX} & k_{XY} \\ k_{YX} & k_{YY} \end{bmatrix} = \begin{bmatrix} \left. \frac{\partial f_x}{\partial X} \right|_0 & \left. \frac{\partial f_x}{\partial Y} \right|_0 \\ \left. \frac{\partial f_y}{\partial X} \right|_0 & \left. \frac{\partial f_y}{\partial Y} \right|_0 \end{bmatrix} \tag{13}$$

$$\begin{bmatrix} c_{XX} & c_{XY} \\ c_{YX} & c_{YY} \end{bmatrix} = \begin{bmatrix} \left. \frac{\partial f_x}{\partial \dot{X}} \right|_0 & \left. \frac{\partial f_x}{\partial \dot{Y}} \right|_0 \\ \left. \frac{\partial f_y}{\partial \dot{X}} \right|_0 & \left. \frac{\partial f_y}{\partial \dot{Y}} \right|_0 \end{bmatrix} \tag{14}$$

where the subscript “0” denotes the quantities in an equilibrium position.

In the present analysis, the dynamic coefficients were numerically calculated using a perturbation method. For a given small displacement or velocity of the journal at an equilibrium position, the dynamic pressure distribution was calculated and the film force components were obtained. The dynamic coefficients were determined from the difference between the force components just obtained, f_x and f_y , and the corresponding ones in the equilibrium position, f_{x0} and f_{y0} , divided by the relevant displacement or velocity. For example, in the case of k_{XX} and k_{YX} , a small displacement Δ_X is only applied while the other infinitesimals are set to zero. With the resulting difference of the oil-film reaction forces due to Δ_X , k_{XX} and k_{YX} are calculated as follows:

$$k_{XX} = \frac{f_x - f_{x0}}{\Delta_X}, k_{YX} = \frac{f_y - f_{y0}}{\Delta_X} \tag{15}$$

In the study, we used 0.001 as the values of the small displacement or velocity.

2.5 Calculation of the Linear Stability Threshold Speed

Figure 4 illustrates a model rotor used for the stability analysis. The rotor is composed of a massless rigid shaft and a disk with a concentrated mass of $2m$ located in the middle, and it is supported by two identical journal bearings at each end.

Considering small vibrations of the rotor at the equilibrium position, the equations of motion of the rotor in the X and Y directions can be written with the dynamic coefficients obtained above as follows:

$$\begin{cases} m\ddot{X} + c_{XX}\dot{X} + c_{XY}\dot{Y} + k_{XX}X + k_{XY}Y = 0 \\ m\ddot{Y} + c_{YX}\dot{X} + c_{YY}\dot{Y} + k_{YX}X + k_{YY}Y = 0 \end{cases} \tag{16}$$

Applying the Routh–Hurwitz stability criterion to the characteristic equation obtained from Eq. (12), the linear stability-threshold shaft speed ω_c for the rigid rotor is obtained in dimensionless form v_c [15],

$$v_c = \frac{v_c}{\sqrt{g/C}} = \sqrt{\frac{a_1 a_3 a_5}{a_1^2 + a_2 a_5^2 - a_1 a_4 a_5}} \tag{17}$$

where g is the acceleration of gravity, and the coefficients a_1 to a_5 are expressed by the following dimensionless dynamic coefficients:

$$\left\{ \begin{array}{l} a_1 = K_{XX}C_{XX} - K_{XY}C_{YX} - K_{YX}C_{XY} + K_{YY} \\ a_3 = C_{XX}C_{YY} - C_{XY}C_{YX} \\ a_3 = C_{XX}C_{YY} - C_{XY}C_{YX} \\ a_4 = K_{XX} + K_{YY} \\ a_5 = C_{XX} + C_{YY} \end{array} \right. \quad (18)$$

In Eq. (14), K_{ij} and C_{ij} ($i, j = x, y$) are the dimensionless stiffness and damping coefficients, respectively, and are defined as follows:

$$K_{ij} = \frac{C}{W} k_{ij}, C_{ij} = \frac{C\omega}{W} c_{ij} \quad (19)$$

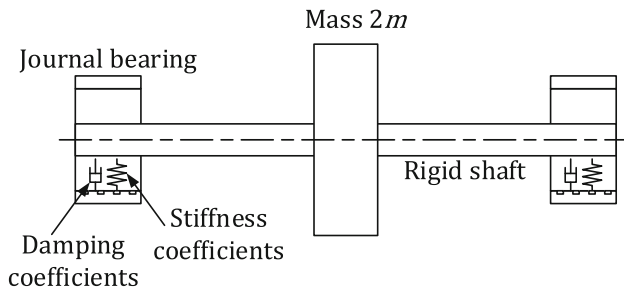


Fig. 4. A model rotor

2.6 Analytical Conditions

The analytical conditions are listed in Table 1. In the analysis, we changed the texture start angle θ_{ts} from 0° to 270° to investigate the position of the textured area under the constant texture angle $\theta_t = 90^\circ$. A fully textured bearing and a smooth bearing were also calculated for comparison. Schematics of the bearing shape used in the study are shown in Fig. 5.

Table 1. Analytical conditions

L/D	1.0
θ_t	90°
θ_{ts}	$0^\circ, 90^\circ, 180^\circ, 270^\circ$
$l_{p\theta}/(2\pi R)$	1/60
l_{pz}/L	1/10
$l_{t\theta}/l_{p\theta} = l_{tz}/l_{pz}$	0.5
h_t/C	1.0

The data obtained in the study was summarized by using the Sommerfeld number S , which is defined by

$$S = \frac{\eta NDL}{W} \left(\frac{R}{C}\right)^2 \tag{20}$$

where N is the rotational speed of shaft.

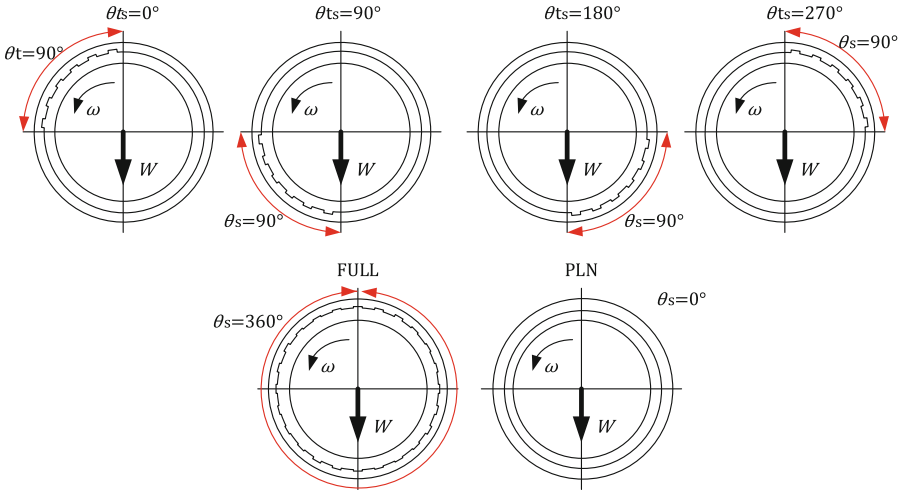


Fig. 5. Schematic diagram of bearing shape used in the analysis

3 Results and Discussion

Figure 6 illustrates the eccentricity ratio ϵ for various Sommerfeld number S . In the figure, the blue and red lines denote the numerical results obtained for partially textured bearings, whereas the black lines for the smooth (PLN) or fully textured ones (FULL). The eccentricity of the partially textured bearings is smaller than that of fully textured one, but larger than that of smooth one for a wide range of S . This means that the reduction of the texture region is effective for improvement of the load carting capacity for the fully textured bearings. In addition, it is difficult to use the surface texturing for the increase of the load carrying capacity. As for the position of the texture region, the eccentricity of $\theta_{ts} = 0^\circ$ and 270° are smaller than those of $\theta_{ts} = 90^\circ$ and 180° . This trend becomes prominent when S is low. The dimples on the loaded region ($90^\circ < \theta < 270^\circ$) on the bearing surface has substantial impact on the load carrying capacity than unloaded region ($\theta < 90^\circ, \theta > 270^\circ$).

From the above results, in order to suppress the reduction of the load carrying capacity the texture region should be formed in the unloaded region. This results qualitatively agree with the results of Tala-Ighil et al. [1] and Brizmer [5].

Figure 7 shows the variations of the attitude angle ϕ . When S is lower, the results of partially textured bearings except 90° are close to that of PLN. As S increases, the influence of θ_{ts} increases. In particular, in the case of $\theta_{ts} = 0^\circ$, ϕ becomes larger than that of PLN.

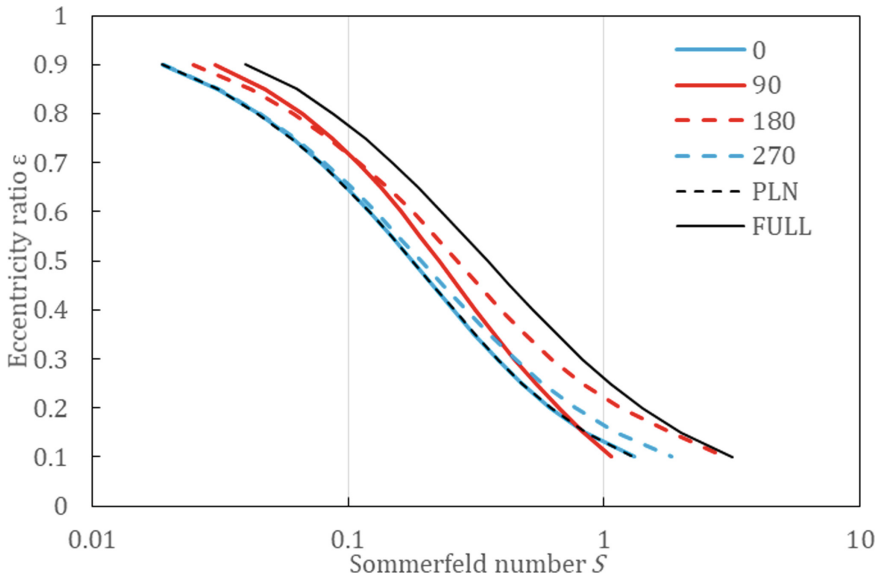


Fig. 6. Variations of eccentricity ratio with Sommerfeld number.

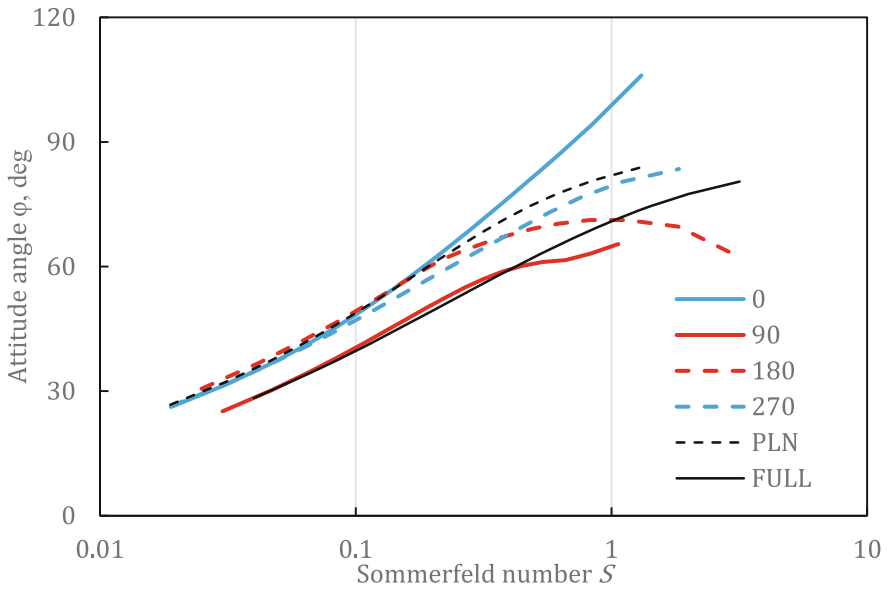


Fig. 7. Variations of attitude angle with Sommerfeld number.

Figure 8 shows a stability chart for the model rotor shown in Fig. 4. It is found that the stability shaft speed of $\theta_{ts} = 270^\circ$ is significantly higher than those of others including FULL and PLN at high Sommerfeld numbers. As the load carrying capacity

of 270° is higher than that for FULL, an appropriate partial texturing can improve both the load carrying capacity and the stability simultaneously. However, the increase of the stability threshold speed in 270° is smaller than the improvement in two lobe bearings with preload factor 0.5, which was calculated on the basis of the stiffness and damping coefficients of the Journal-bearing Databook [16]. On the other hand, the stability shaft speeds for 0° , 90° , 180° do not exceed that of FULL. Even on the same unloaded region, stability characteristics of 0° and 270° are entirely different.

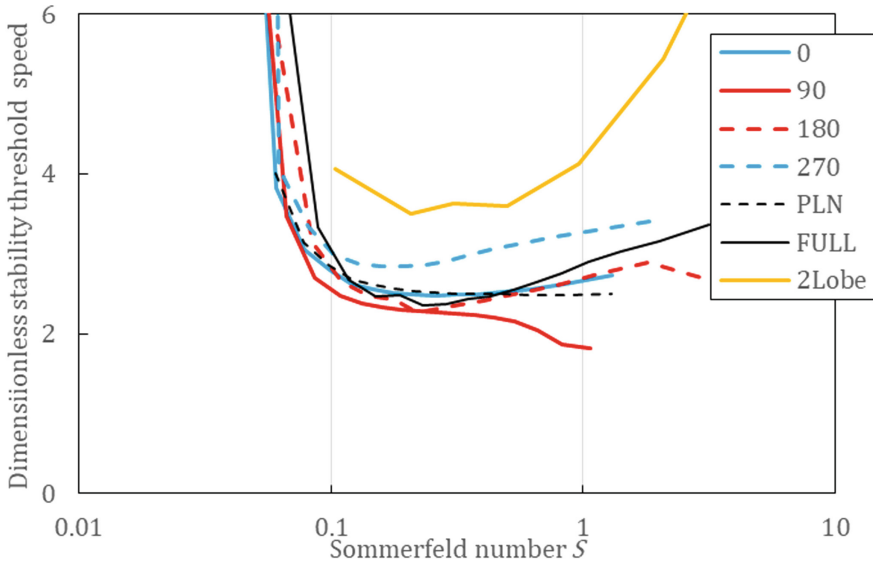


Fig. 8. Stability chart of a rigid rotor supported in the two identical partially textured bearings

Figures 9 and 10 show the stiffness and damping coefficients respectively. These values are used to create the stability chart shown in Fig. 8. Focusing on the results of 270° which have high stability threshold speeds, two specific features seem to exist at high Sommerfeld number. One is that the magnitude of the cross-coupling stiffness coefficient K_{YX} is relatively smaller than those of the other partially textured bearings at higher Sommerfeld numbers. The other is the direct damping coefficients C_{XX} and C_{YY} are larger than those of FULL at higher Sommerfeld numbers. The decrease of the cross-coupling stiffness coefficients and the increase of the direct damping coefficients is known to improve the stability characteristics of the rotor system. Hence the stability of 270° is relatively higher than the others.

In the case of 180° , some stiffness and the damping coefficients change discontinuously at high Sommerfeld number. This is due to the large step of the Sommerfeld number.

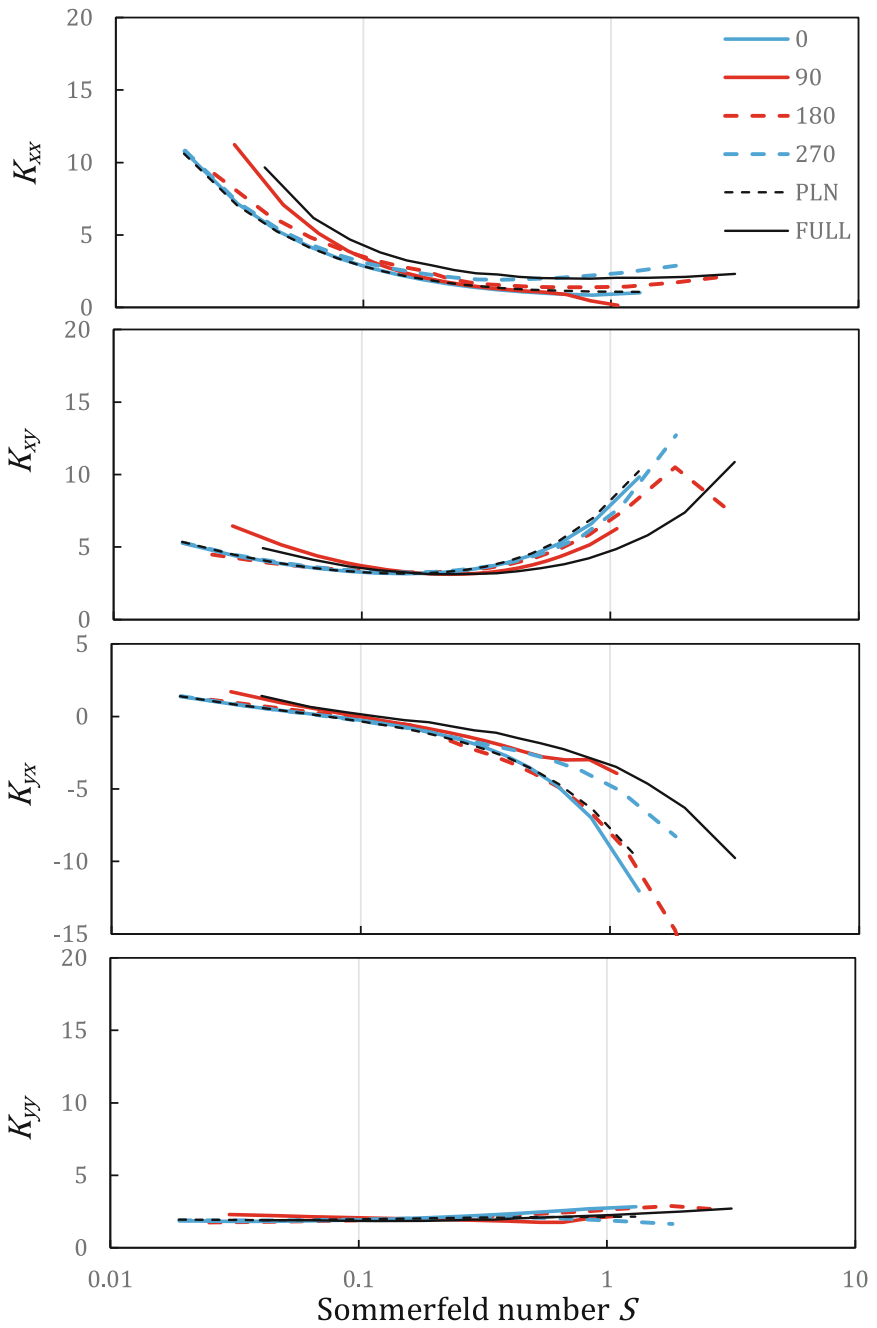


Fig. 9. Stiffness coefficients for partially textured bearings

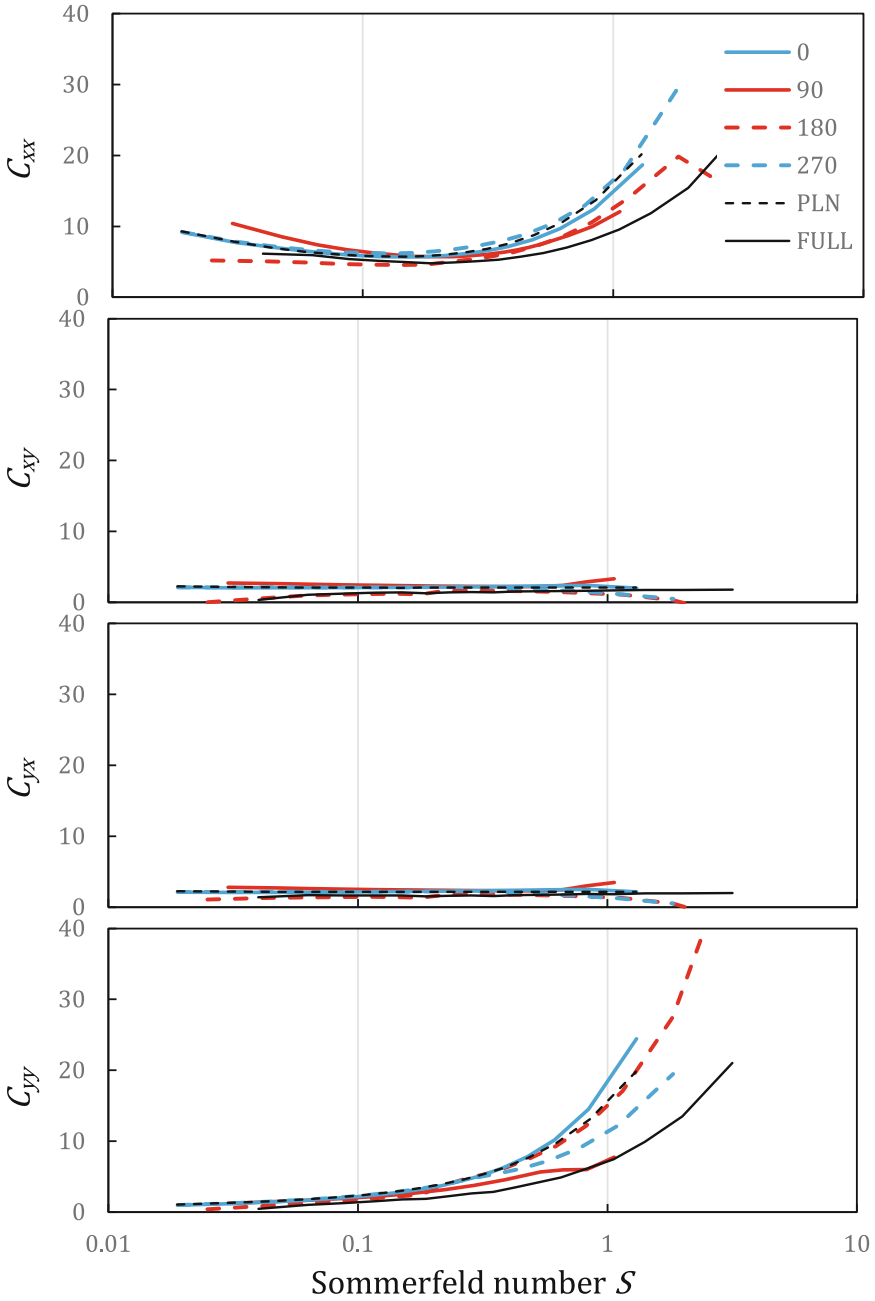


Fig. 10. Damping coefficients for partially textured bearings

4 Conclusions

In the study, we investigated the effect of the texturing region on the static and dynamic characteristics of partially textured bearings theoretically. We performed numerical calculations to obtain the load carrying capacity and the stiffness and damping coefficients of the oil film and the linear stability-threshold shaft speed of the rigid rotor supported by textured bearings by changing the start angle of the texture region.

1. An appropriate partial texturing formed on the bearing surface can improve both the load carrying capacity and the stability characteristics simultaneously.
2. The start angle of the texture region should be set at 270 from the top of the bearing in the rotating direction to improve the bearing characteristics.

References

1. Tala-Ighil, N., Fillon, M., Maspeyrot, P.: Effect of textured area on the performances of a hydro-dynamic journal bearing. *Tribol. Int.* **44**, 211–219 (2011)
2. Ausas, R., Ragot, P., Leiva, J., Jai, M., Bayada, G., Buscaglia, G.C.: The impact of the cavitation model in the analysis of microtextured lubricated journal bearings. *Trans. ASME J. Tribol.* **129**(4), 868–875 (2007)
3. Cupillard, S., Cervantes, M., Glavatskih, S.: A CFD study of a finite textured journal bearing. In: IAHR 24th Symposium on Hydraulic Machinery and Systems, Brazil, October 27–31 (2008)
4. Tala-Ighil, N., Maspeyrot, P., Fillon, M., Bounif, A.: Hydrodynamic effects of texture geometries on journal bearing surfaces. *The annals of university “Dunareade Jos” of Galati, Fascicle VIII, ISSN1221-4590, Tribology, XIV2008*, pp. 47–52 (2008)
5. Brizmer, V., Kligerman, Y.: A laser surface textured journal bearing. *Trans. ASME J. Tribol.* **134**(3), 031702 (2012)
6. Kango, S., Singh, D., Sharma, R.K.: Numerical investigation on the influence of surface texture on the performance of hydrodynamic journal bearing. *Meccanica* **47**(2), 469–482 (2012)
7. Kango, S., Sharma, R.K., Pendey, R.K.: Comparative analysis of textured and grooved hydrodynamic journal bearing. *Proc. Inst. Mech. Eng. Part J: J. Eng. Tribol.* **228**(1), 82–95 (2014)
8. Mishra, S., Choudhury, A., Sahu, S.: CFD investigation of influence of reverse textures on bearing surface of a journal bearings. *J. Appl. Fluid Mech.* **7**(3), 395–399 (2014)
9. Tala-Ighil, N., Fillon, M.: A numerical investigation of both thermal and texturing surface effects on the journal bearings static characteristics. *Tribol. Int.* **90**, 228–239 (2015)
10. Meng, F.M., Zhang, L., Liu, Y., Li, T.T.: Effect of compound dimple on tribological performance of journal bearing. *Tribol. Int.* **91**, 99–110 (2015)
11. Yamada, H., Taura, H., Kaneko, S.: Static characteristics of journal bearings with square dimples. *Trans. ASME J. Tribol.* **139**(5), 051703-051703-11 (2017)
12. Yamada, H., Taura, H., Kaneko, S.: Numerical and experimental analyses of the dynamic characteristics of journal bearings with square dimples. *Trans. ASME J. Tribol.* **140**(1), 011703-011703-13 (2017)
13. Constantinescu, V.N., Galetuse, S.: Pressure drop due to inertia forces in step bearings. *Trans. ASME J. Tribol.* **98**, 167–174 (1976)

14. Arghir, M., Alsayed, A., Nicolas, D.: The finite volume solution of the reynolds equation of lubrication with film discontinuities. *Int. J. Mech. Sci.* **44**, 2119–2132 (2002)
15. Gasch, R., Pfützner, H.: *Rotordynamik Eine Einführung*. Springer, Berlin (1975)
16. Someya, T.: *Journal-Bearing Databook*. Springer, Berlin (1989)